Supporting information

Engineering Interfacial Water Microenvironment to Accelerate Proton Transfer for Acidic Oxygen Evolution at High-Potential

Author: Xiaolong Liang,[a] Ke Xu,[a] Hengkun Yu,[a] Xu Ge,[a] Zhiwen Liu,[a] Xueliang Mu,[d] Shaoke Zhang,[b] Jake M. Yang[c] and Jinxuan Liu[a, d, e]*

[a] State Key Laboratory of Fine Chemicals, Dalian University of Technology, 116024 Dalian, China.

[b] Advanced Institute for Ocean Research, Southern University of Science and Technology, 1088, Xueyuan Blvd., Nanshan District, Shenzhen, Guangdong, P.R. China.

[c] Centre for Sustainable Materials Processing, School of Chemistry, University of Leicester, University Road, Leicester, LE1 7RH, UK.

[d] Leicester International Institute, Dalian University of Technology, 116024 Dalian, China.

[e] Liaoning Binhai Laboratory, 116023 Dalian, China

* Jinxuan Liu - State Key Laboratory of Fine Chemicals, Dalian University of Technology, 116024 Dalian, China.
E-mail: jinxuan.liu@dlut.edu.cn

Experimental section

Materials and Methods

Preparation of chemicals and materials

Cobalt nitrate hexahydrate ($Co(NO_3)_2 \cdot 6H_2O$, 99.9%) and cadmium nitrate tetrahydrate ($Cd(NO_3)_2 \cdot 4H_2O$, 99.9%) are purchased from Aladdin (country). Ethanol (CH_3CH_2OH, purity ≥99.7%) is supplied by Tianjin Jiangtian Chemical Technology Co., LTD. Commercial carbon paper (CP) purchased from Suzhou Sinero Technology Co., LTD. The H_2SO_4 was purchased from Sigma Aldridge (country). Purify deionized water (18.2 ΩM cm, 25°C) using a specific laboratory water purification system. All of the above chemicals and reagents were used as supplied without purification.

Preparation of clean Carbon paper

A piece of carbon paper (CP) of 1 × 2 cm^2 was first ultrasonicated in an 18.4 M H_2SO_4 solution for 1.5 h to remove surface impurities andenhance the hydrophilicity of the CP, then was ultrasonicated in wateifor a further 0.5 h to remove residual sulfuric acid on the surface. The ultrasound bath used was SK3200LHC, 53 Hz.

Synthesis of CdO-$Co_{3-x}Cd_xO_4$/CP

Firstly, different proportions of $Co(NO_3)_2 \cdot 6H_2O$ and $Cd(NO_3)_2 \cdot 4H_2O$ were configured, summing to a total of 1 mmol. The mixture was then dissolved in 50 ml of deionized water, followed by sonication for 10 minutes, and the fully dissolved solution was used as an electrolyte. The traditional three-electrode system is used for electrodeposition, with the treated carbon paper as the working electrode, the Pt wire electrode as the opposite electrode and the saturated calomel electrode as the reference electrode. The electrodeposition was then carried out at a current density of -20 mA cm^{-2}, and the deposition time was 10 minutes. The obtained heterostructure catalyst was dried for 6 h. Finally, the dry catalyst was annealed for 4 hours at 400 °C. CdO-$Co_{3-x}Cd_xO_4$ and Co_3O_4 were loaded at 2.3 mg/cm^{-2} and 2.1 mg/cm^{-2}, respectively. All electrochemical performances were measured based on mass-normalized current density.

The specific different proportions of $Co(NO_3)_2 \cdot 6H_2O$ and $Cd(NO_3)_2 \cdot 4H_2O$ used in the synthesis were 1) 0.8 mmol and 0.2 mmol, 2) 0.7 mmol and 0.3 mmol, 3) 0.5 mmol and 0.5mmol. To electrodeposit Co_3O_4/CP particles, 1mmol of $Co(NO_3)_2 \cdot 6H_2O$ was used in the absence of any added $Cd(NO_3)_2 \cdot 4H_2O$.

Materials characterization

X-ray diffractometer (XRD, SmartLab 9kW, Japan) with CuKα radiation (λ = 1.5418 nm) was used to record crystallographic information of the catalyst. Field emission scanning electron microscope (SEM, FEI Nova Nano SEM 450) and transmission electron microscope (TEM, JEM-F200) were used to identify the morphology and map the elemental distribution across the surface of the catalyst. X-ray photon energy spectroscopy (XPS, Axis Supra+) was used to determine the redox state of the sample surface. Raman spectra were recorded using LabRam HR spectrometer (Horiba Jobin Yvon) with a 50X objective microscope. The excitation line was 638 nm with a power of 2.4 mW.

Electrochemical measurements

All electrochemical tests were performed on an electrochemical workstation (Princeton VersaSTAT 3F) at room temperature in a traditional three-electrode system using a Pt wire (Φ = 1 mm) as the counter electrode, the as-prepared catalysts and carbon paper (effective geometric area: 1 x 1 cm^2) as the working electrode, and a Ag/AgCl electrode as the reference electrode. 0.5 M H_2SO_4 was used as the electrolyte for all electrochemical tests.

Electrocatalytic test

All the measured potentials vs Ag/AgCl were converted to the potential vs reversible hydrogen electrode (RHE) potential ($E_{RHE} = E_{Ag/AgCl} + 0.197\ V + 0.059\ V \times pH$)

Cyclic voltammetry (CV) measurements

CV experiments were performed in 0.5 M H_2SO_4 (pH = 0.3) aqueous solution using a three-electrode system connected to an electrochemical workstation at room temperature. Ag/AgCl electrode was denoted as the reference electrode and a platinum wire electrode (Φ1 mm) was used as the counter electrode. Before conducting the LSV test, perform a CV cycle for 10 times (CV range 1~2 V vs Ag/AgCl, scan rate 50 mV s-1) to ensure the stability of the catalyst.

Linear sweep voltammetry (LSV) measurements

The measurement conditions of LSV are identical to those of CV. The OER activity of the material was measured by LSV with a scan rate of 5 $mV \cdot s^{-1}$ with iR compensation (IR compensation is automatically performed by the electrochemical workstation, compensating for 80%). We used a reverse scan method, from high potential to low potential, to avoid the overlap of oxidation peaks between metal ion and water, which will ensure the accuracy of electrochemical data. The overpotentials (η) at 10 $mA \cdot cm^{-2}$ were calculated using $\eta_{10} = E_{RHE} - 1.23\ V$. Tafel slopes were calculated using the LSV

curves by the Tafel equation: $\eta = b \log j + a$, *where* η represents overpotential; j represents current density; a is the constant; and b stands for the Tafel slope.

Electrochemical active surface area (ECSA) measurements

CV tests with different scan rates from 20 to 120 $mV \cdot s^{-1}$ in the potential range of 0.8 - 0.9 V (νs. RHE) was performed to evaluate the electrochemical active surface area (ECSA) of the electrocatalysts. By plotting the capacitive currents (J_{anodic} - $J_{cathodic}$) at 0.85 V (νs. RHE), the double-layer capacitance (C_{dl}) is equal to half of the slope. The ECSA of the samples is calculated from the C_{dl} according to the equation: ESCA = C_{dl}/C_s, where C_s = 0.040 mF cm^{-2} in H_2SO_4.

Stability tests

Chronopotentiometry (CP) was performed at 10 $mA \cdot cm^{-2}$ to evaluate the stability of the electrocatalysts without iR correction.

In situ electrochemical impedance spectroscopy (EIS) test

In this experiment, 0.5 M H_2SO_4 solution was selected as the electrolyte, and the test potential was gradually increased from 1.0 V to 1.7 V, which covered the possible electrochemical processes of catalysts at different potentials. The acquisition frequency extends from 10^{-1} Hz to 10^4 Hz. Ensure the capture of various electrochemical phenomena, including charge transfer resistance, double-layer capacitance, and diffusion processes.

X-ray absorption spectroscopy

Transmission XAS measurements were performed on a laboratory device (easyXAFS300+, easyXAFS LLC), which is based on Rowland circle geometries with spherically bent crystal analyzers (SBCA) and a silicon drift detector. Si (5,3,3) was used for Co K-edge measurement. The powder samples were thoroughly ground and mixed with Cellulose (or Boron Nitride) using an agate mortar and pestle and pressed into Ø = 10 mm pellets. The pressed pellets were then sandwiched by Kapton tapes.

In situ ATR-SEIRAS (Surface Enhanced Infrared Absorption Spectroscopy)

The ATR-SEIRAS experiments were carried out using a BRUKER VERTEX 80v spectrometer equipped with an MCT detector cooled by liquid nitrogen. In situ ATR-SEIRAS experiments were performed in a customized spectroelectrochemical cell obtained from Shanghai Yuanfang Technology Company. For spectroscopic analysis, 10 mg of catalyst nanoparticles were dispersed in a mixture of 140 μL ethanol and 60 μL of 5% Nafion under ultrasonication for 30 minutes to produce an ink solution. The ink solution was then loaded onto a silicon ATR crystal coated with Au film, serving

as the working electrode, while an Ag/AgCl electrode and Pt wire were utilized as reference and counter electrodes, respectively. The ATR SEIRAS spectrum obtained with no applied potential was considered as background, and all spectra in the figures were acquired by subtracting the background spectrum.

Kinetic Isotope Effect (KIE) Study

Electrolyte Preparation: Protic electrolytes were prepared using high-purity H_2O (0.5 M H_2SO_4). Deuterated electrolytes were prepared using D_2O (≥98 at% D; 0.5 M D_2SO_4 in D_2O). Electrochemical Measurements: All experiments were conducted in an Ar-purged cell. An Ag/AgCl electrode was used as the reference, and a Pt mesh as the counter electrode. Cyclic voltammetry (CV) and linear sweep voltammetry (LSV) were performed at scan rates of 50 mV s^{-1} and 5 mV s^{-1}, respectively. All potentials were iR-corrected and converted to the RHE or RDE scale, considering the thermodynamic potential difference between H_2O and D_2O.

$$E(V\ vs.\ RHE) = E(V\ vs.Ag/AgCl) + 0.197 + 0.059\ pH$$

$$E(V\ vs.\ RDE) = E(V\ vs.Ag/AgCl) + 0.197 + 0.013 + 0.059\ pD$$

KIE Evaluation: The KIE was calculated as the ratio of kinetic current densities in H_2O and D_2O at the same overpotential (η):

$$KIE = \frac{k_{H2O}}{k_{D2O}} = \frac{J_{H2O}}{J_{D2O}}$$

Calculation method

Establishment of Co_3O_4 base: The Co_3O_4 cell model was established, the (311) crystal face was cut, and the Castep Geometry Optimization module was used to optimize the cell. The method was as follows: Generalized Gradient Approximation is used to calculate the PBE potential function. The cut-off energy is 571.40 eV, cut-off stress is 0.03 eV/A, critical pressure is 0.05 GPa and cut-off displacement is 0.001 A. The energy convergence standard was 1.0 e-6 eV, the maximum number of cycles was 200, the convergence algorithm was LBGFS function, the pseudopotemia was OTFG ultrasoft, and the optimized substrate thickness was 3.27 A. Heterostructure establishment: Cd doping is performed on the (311) crystal surface of Co_3O_4 established above, according to Co: With the ratio of Cd=8:1, the Co was randomly doped by 1/8 to form the (311) crystal surface of $Co_{2.625}Cd_{0.375}O_4$, and the structure was optimized by Castep Geometry Optimization. Generalized Gradient Approximation is used for PBE potential function, and the parameter Settings are the same as in 1.

Establishment of the heterostructure base: CdO-$Co_{2.625}Cd_{0.375}O_4$ heterostructure was formed with the standard CdO cell and vacuum layer, and the thickness of the heterojunction was 8.95 A; Castep's Geometry Optimization module was used to optimize the adsorption models with Co-O as the action site, and the adsorption configurations of CdO-$Co_{2.625}Cd_{0.375}O_4$-H_2O and Co_3O_4-H_2O were optimized respectively. Adsorption energy $E_{ads}=E_{total}-E_{crystal}-E_{H2O}$; Establishment of the liquid phase model: Use Amorphous cell module to set up the box containing solute and solvent. The aqueous solution is 0.5 mol/L H_2SO_4 solution, the side length of the box is 32.4 A, and the force field is COMPASSIII.

GULP module was used to add 1.7 V and 1.6 V into the material in the direction of Layer model (001), and Forcite's Geometry Optimization module was used to optimize the four Layer models. The convergence of energy and force values is 2.0e-5 kcal/mol and 0.001 kcal/mol/A, respectively. The convergence of displacement is 1.0e-5. COMPASSIII is used in the force field, and the maximum number of cycles is 1000. In the case of fixed base, the Dynamic module is used for molecular dynamics simulation under electric field. The ensemble is NVT ensemble, the step size is 0.5 fs, the total balance time is 200 ps, the total number of simulation steps is 400000, and the trajectory snapshot is output every 1000 steps. The cut-off radius of the van der Waals force is 15.5 A, and the force field uses COMPASSIII; The temperature was set to 293.15 K, and the four samples were given a primary molecular thermal motion trajectory of 200 ps, using Perl. The number of hydrogen bonds and the distribution of hydrogen bond concentration along the Z axis of the language statistical dynamics state process; Use Forcite analysis to output the radial distribution function of Co-O(H_2O), O(H_2O)-O(H_2O), O(H_2O)-H(H_2O) and H(H_2O)-H(H_2O). The radial distribution function truncates the distance range from 0 to 20 A and the distance interval is 0.02 A.

Figures and Tables

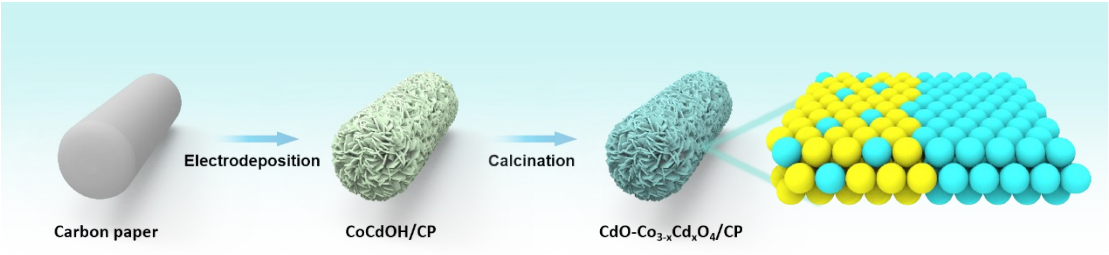

Figure S1. Scheme for the synthesis of CdO-$Co_{3-x}Cd_xO_4$/CP.

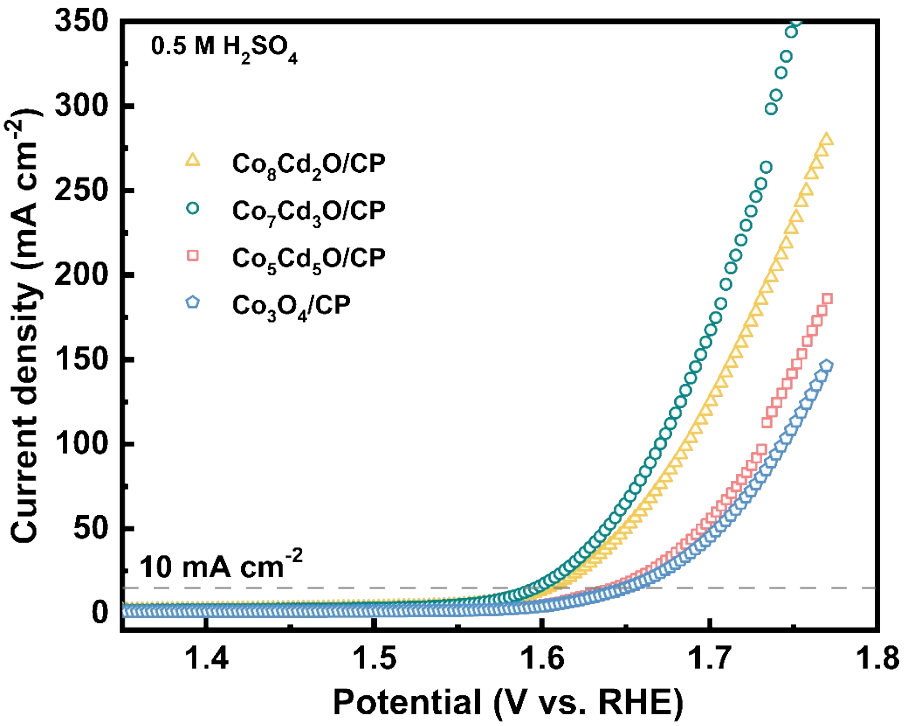

Figure S2. LSV curves of Co_8Cd_2O/CP, Co_7Cd_3O/CP ,Co_5Cd_5O/CP and Co_3O_4/CP in 0.5 M H_2SO_4 solution.

The linear scanning voltammograms (LSV) of the catalysts with varying Co/Cd ratios were studied in 0.5 M H_2SO_4 to evaluate their catalytic performance. As illustrated in Figure S10, the Co_7Cd_3O/CP catalyst exhibited the highest catalytic activity, demonstrating an overpotential of 346 mV at a current density of 10 mA cm^{-2}. This performance surpassed that of Co_8Cd_2O/CP, which had an overpotential of 370 mV, and Co_5Cd_5O/CP, which recorded 405 mV. The significantly lower overpotential of Co_7Cd_3O/CP compared to reported values underscores its superior catalytic activity. Further insights into the reaction kinetics were obtained through Tafel analysis (Figure S11). The Co_7Cd_3O/CP catalyst showed the fastest oxygen evolution reaction (OER) kinetics, as evidenced by the smallest Tafel slope of 82.1 mV dec^{-1}. This value was lower than those of Co_8Cd_2O/CP (87.3 mV dec^{-1}) and Co_5Cd_5O/CP (98.4 mV dec^{-1}), indicating enhanced efficiency in the OER mechanism. The electrochemically active surface areas (ECSAs) of the catalysts were quantified using double-layer capacitance (C_{dl}), with results presented in Figures S4 and S5. The Co_7Cd_3O/CP

catalyst exhibited the largest C_{dl} value of 9.27 mF cm^{-2}, surpassing Co_8Cd_2O/CP (8.76 mF cm^{-2}) and Co_5Cd_5O/CP (4.28 mF cm^{-2}). This higher C_{dl} value suggests that Co_7Cd_3O/CP can expose more active sites, contributing to its enhanced catalytic performance. To enhance understanding of the effect of heterostructures on catalytic performance, we will refer to the Co_7Cd_3O/CP catalyst as CdO-$Co_{3-x}Cd_xO_4$/CP in the following discussion.

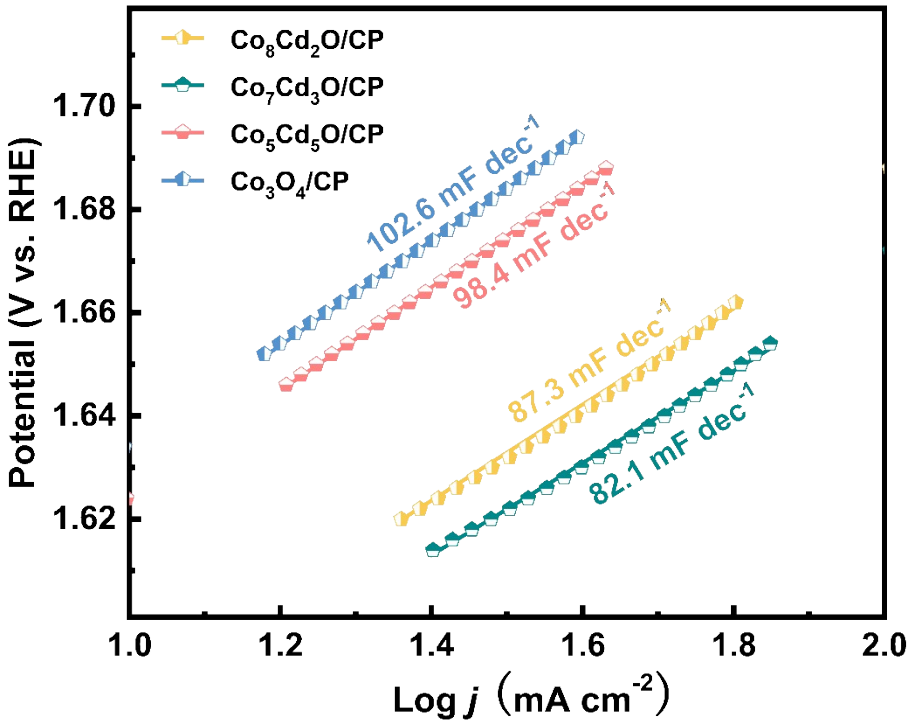

Figure S3. Tafel plots of Co_8Cd_2O/CP, Co_7Cd_3O/CP, Co_5Cd_5O/CP and Co_3O_4/CP according to the LSV curves.

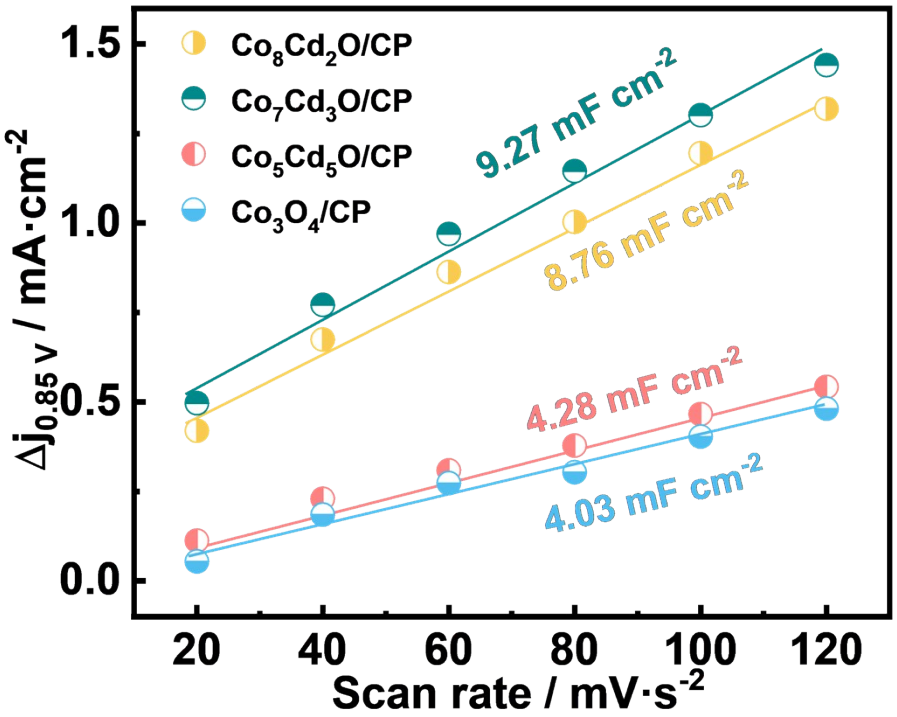

Figure S4. Double-layer capacitances of the Co_8Cd_2O/CP, Co_7Cd_3O/CP and Co_5Cd_5O/CP.

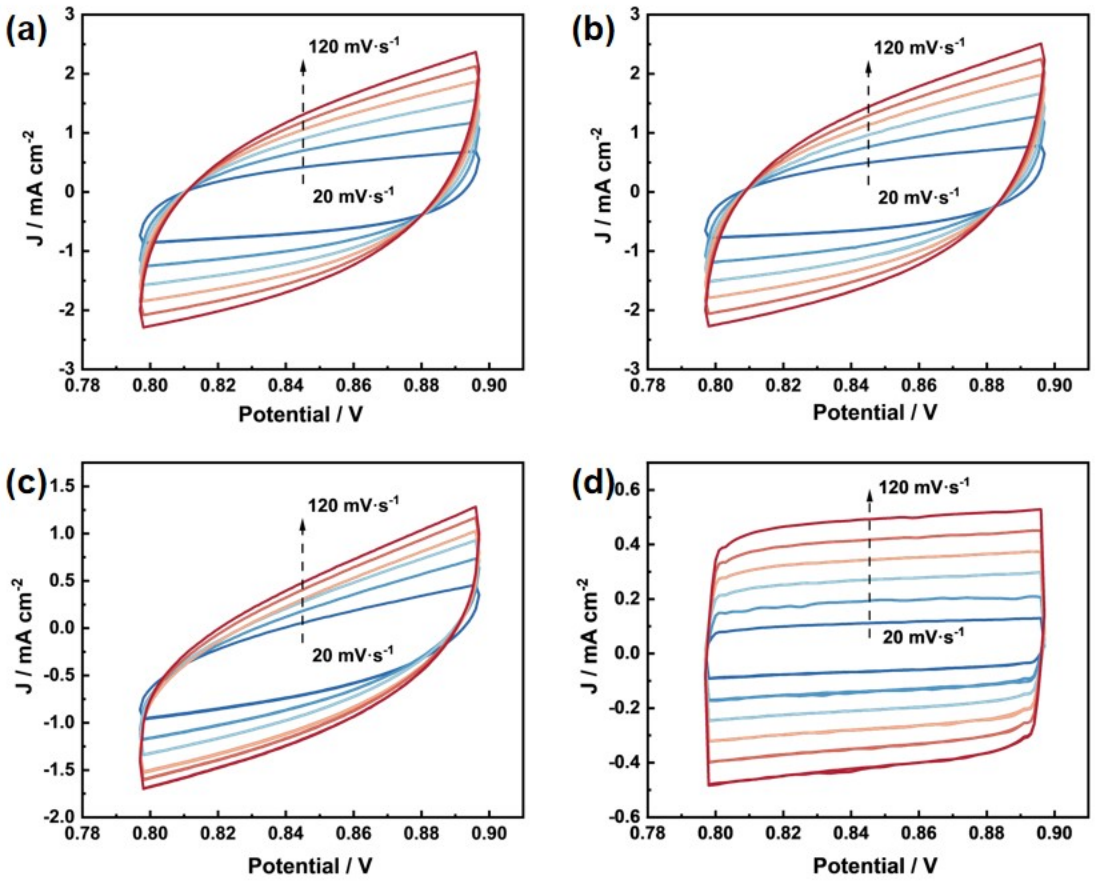

Figure S5. CV curves of (a) Co_8Cd_2O/CP, (b) Co_7Cd_3O/CP, (c) Co_5Cd_5O/CP, and (d) Co_3O_4 (with varying scan rates: 20, 40, 60, 80, 100 and 120 $mV \cdot s^{-1}$) in 0.5 M H_2SO_4.

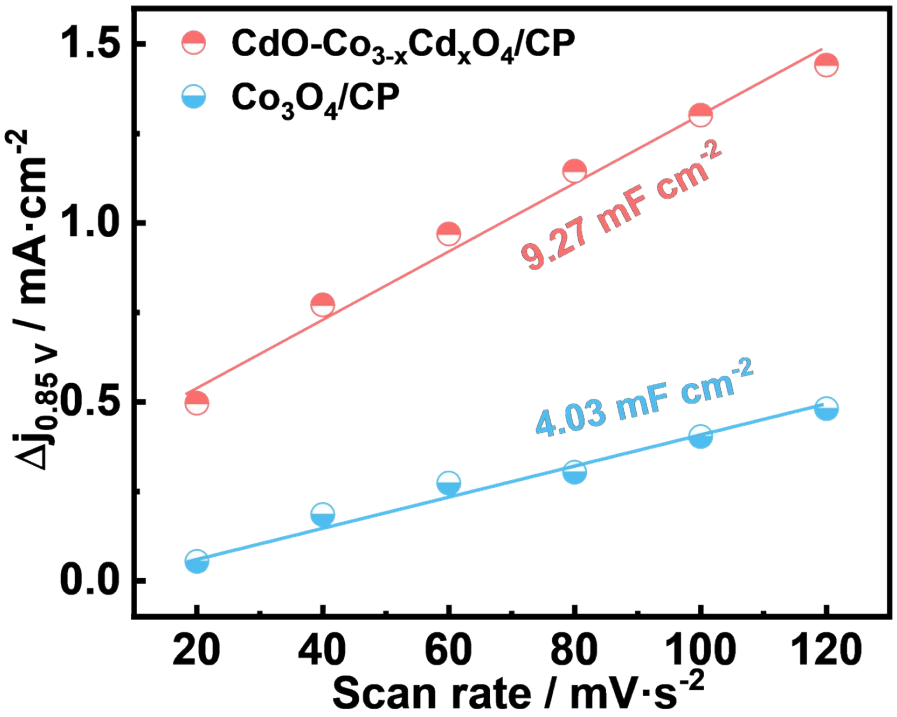

Figure S6. Double-layer capacitances of the CdO-$Co_{3-x}Cd_xO_4$/CP and Co_3O_4/CP.

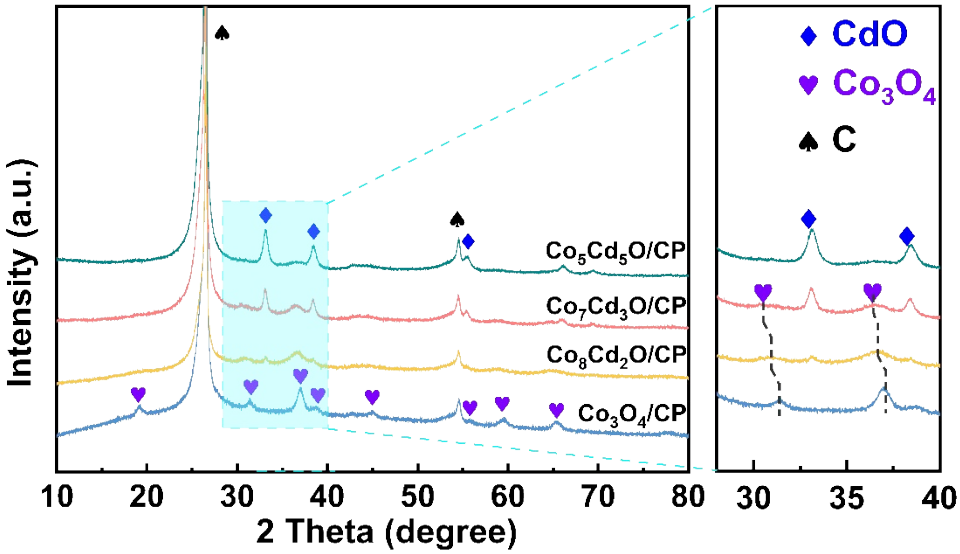

Figure S7. XRD patterns of Co_3O_4/CP, Co_8Cd_2O/CP, Co_7Cd_3O/CP and Co_5Cd_5O/CP.

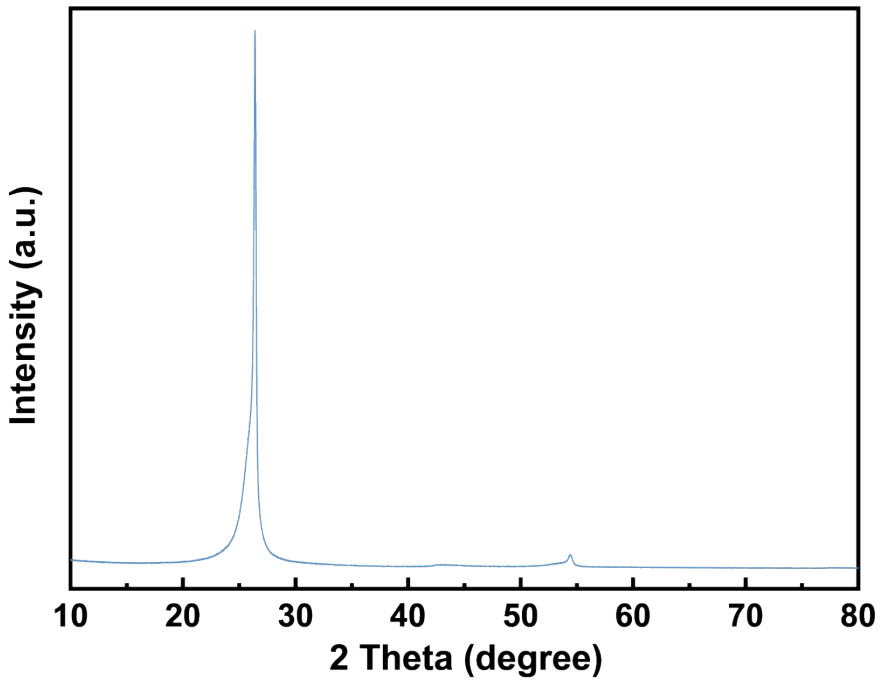

Figure S8. XRD pattern of pure carbon paper.

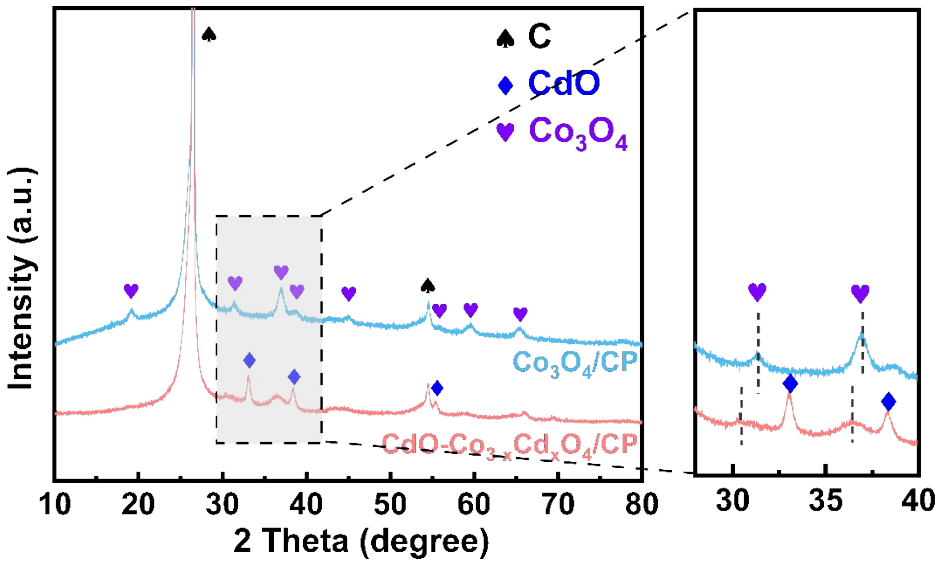

Figure S9. XRD patterns of CdO-$Co_{3-x}Cd_xO_4$/CP and Co_3O_4.

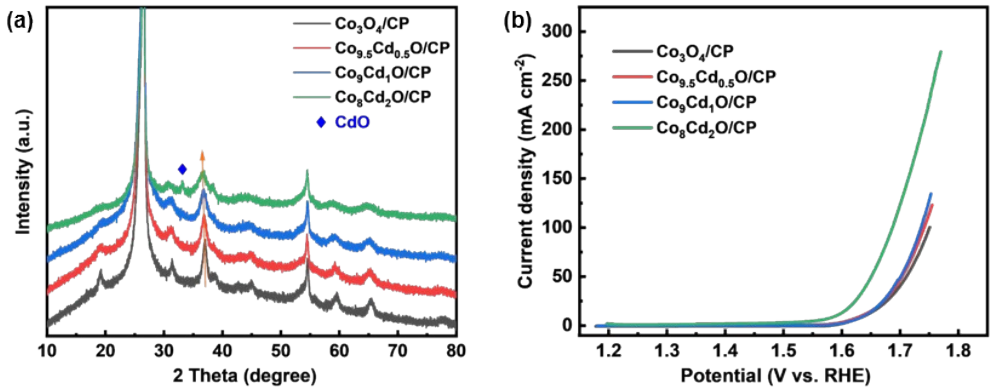

Figure S10. (a) XRD pattern of Co_3O_4/CP, $Co_{9.5}Cd_{0.5}O$/CP, Co_9Cd_1O/CP and Co_8Cd_2O/CP; (b) LSV of Co_3O_4/CP, $Co_{9.5}Cd_{0.5}O$/CP, Co_9Cd_1O/CP and Co_8Cd_2O/CP.

To exclude the possibility that the performance enhancement originates solely from cation doping, we synthesized a trace-Cd-doped control sample (Cd-Co_3O_4). XRD analysis confirms the formation of a solid solution without any detectable CdO phase (Figure S10a). Electrochemical tests reveal that this control sample exhibits negligible activity improvement compared to pristine Co_3O_4 (Figure S10b). In contrast, when the Co/Cd molar ratio reaches 8:2, characteristic diffraction peaks of CdO are clearly observed in the XRD pattern, accompanied by a significant surge in OER performance for the Co_8Cd_2O/CP sample. These results collectively demonstrate that the electronic modulation from doping alone is insufficient to drive the high-potential OER, thereby highlighting the indispensable role of the heterostructure interface.

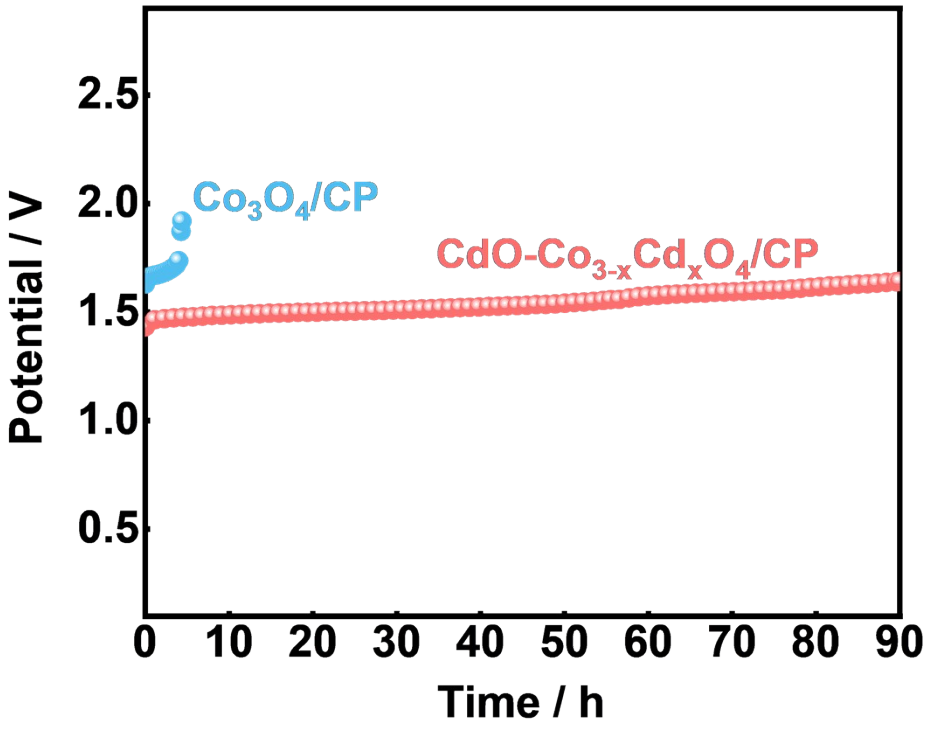

Figure S11. Chronopotentiometric curves of CdO-$Co_{3-x}Cd_xO_4$/CP and Co_3O_4/CP at current density of 10 mA cm^{-2}.

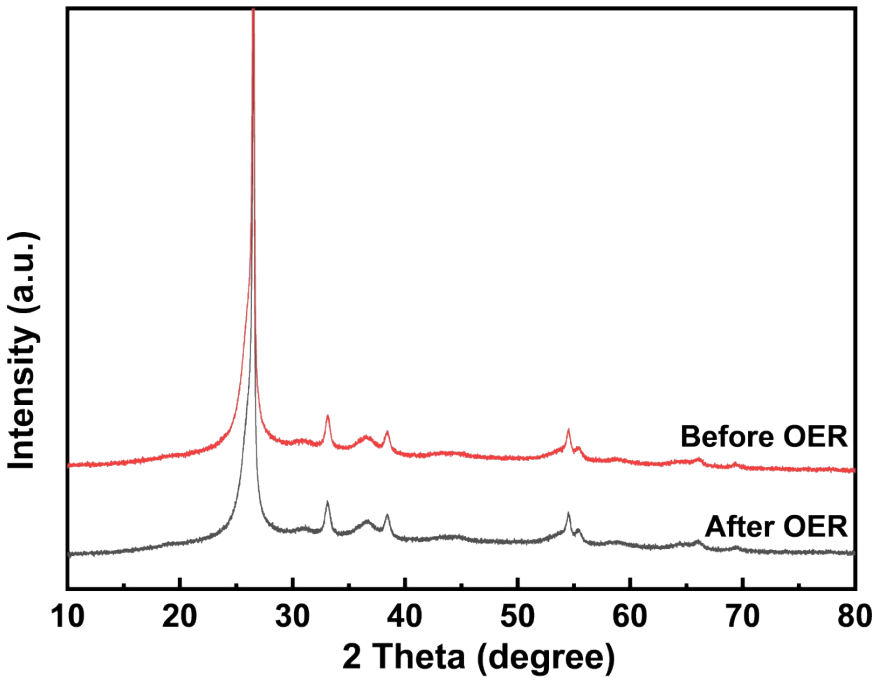

Figure S12. XRD patterns of before (red) and after OER test (black) CdO-$Co_{3-x}Cd_xO_4$/CP in 0.5 M H_2SO_4.

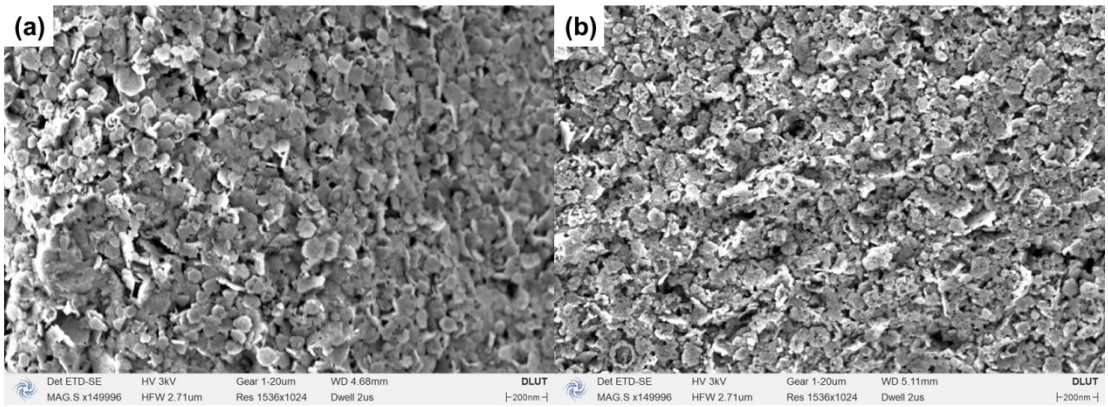

Figure S13. SEM images of before (a) and after OER test (b) CdO-$Co_{3-x}Cd_xO_4$/CP in 0.5 M H_2SO_4.

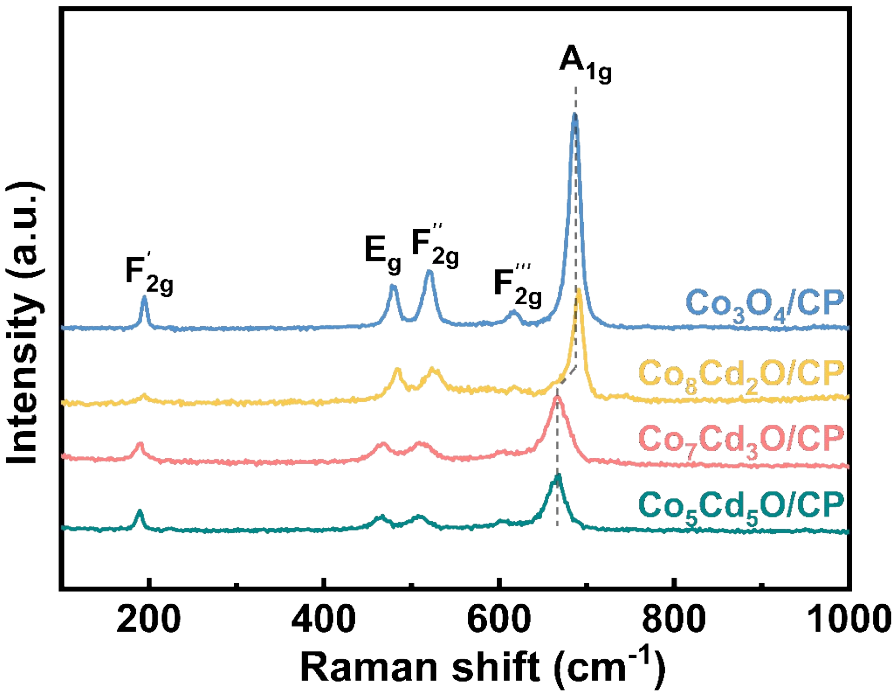

Figure S14. Raman spectrum of (a) Co_3O_4/CP, (b) Co_8Cd_2O/CP, (c) Co_7Cd_3O/CP and (d) Co_5Cd_5O/CP.

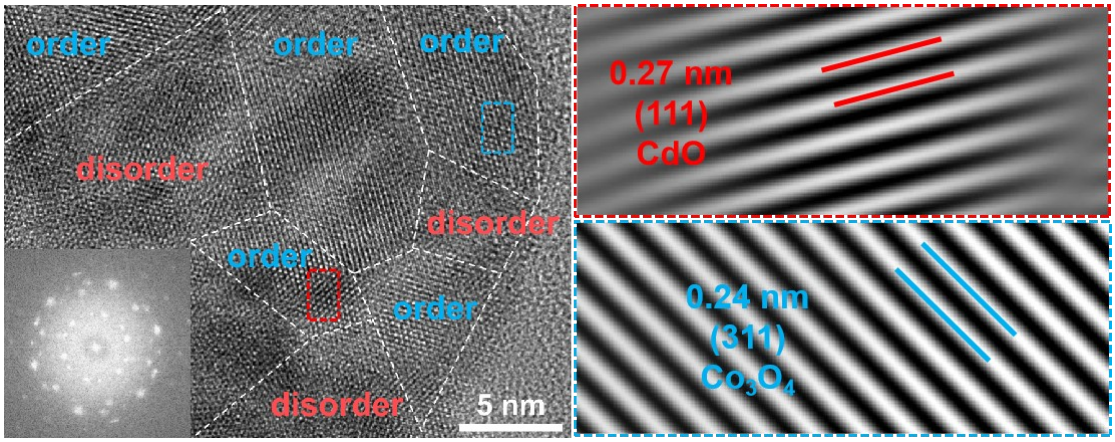

Figure S15. TEM images of CdO-$Co_{3-x}Cd_xO_4$. IFFT images of CdO-$Co_{3-x}Cd_xO_4$ at different areas for recognizing CdO (Red Frame) and Co_3O_4 (Blue Frame).

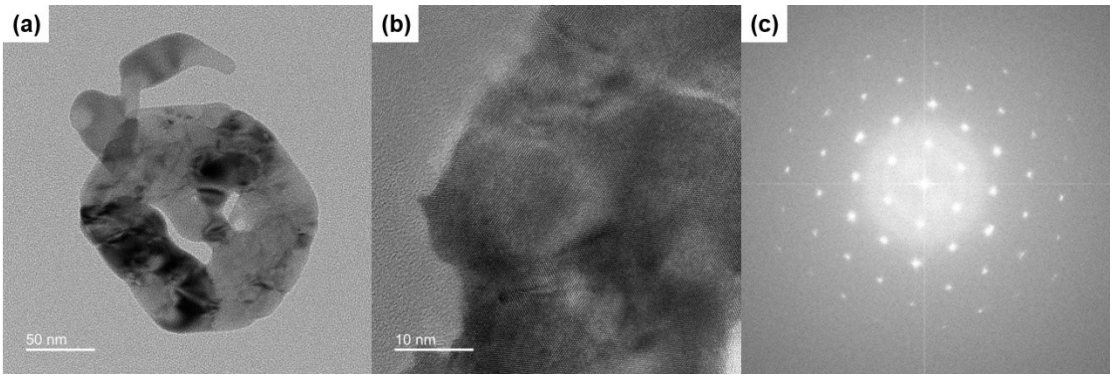

Figure S16. TEM image of single phase Co_3O_4 (a, b) and FFT image of single phase Co_3O_4(c).

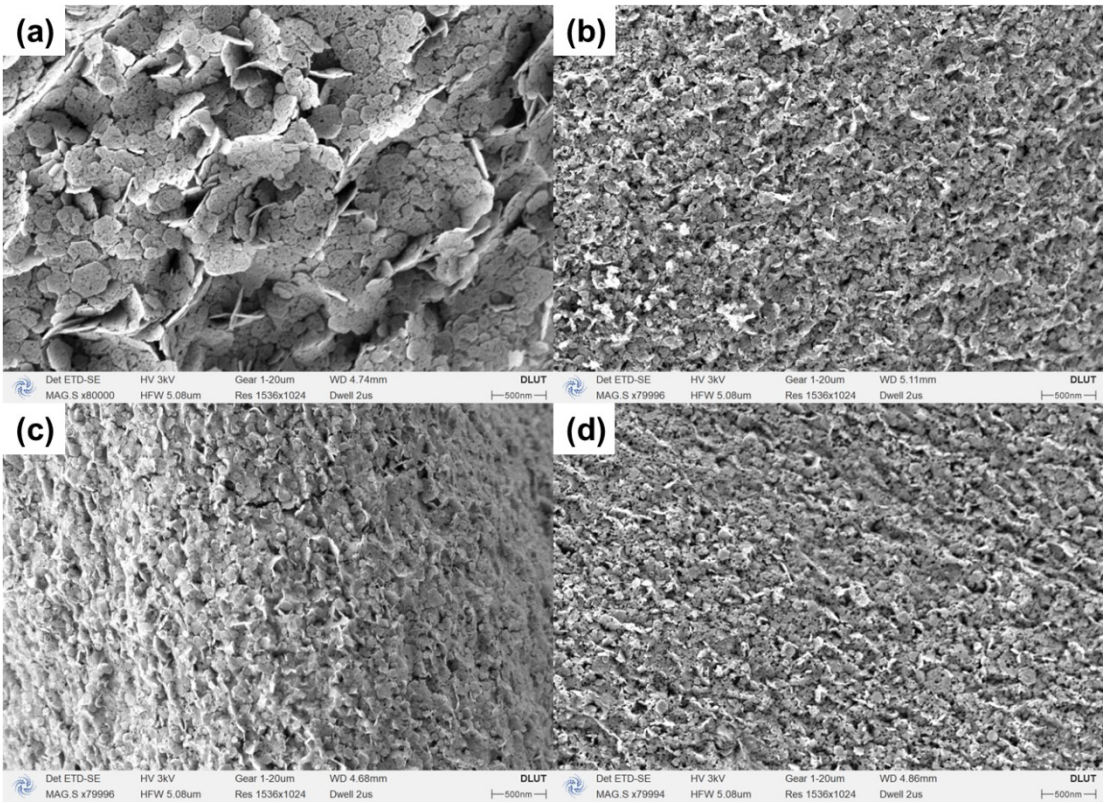

Figure S17. SEM images of (a) Co_3O_4/CP, (b) Co_8Cd_2O/CP, (c) Co_7Cd_3O/CP and (d) Co_5Cd_5O/CP.

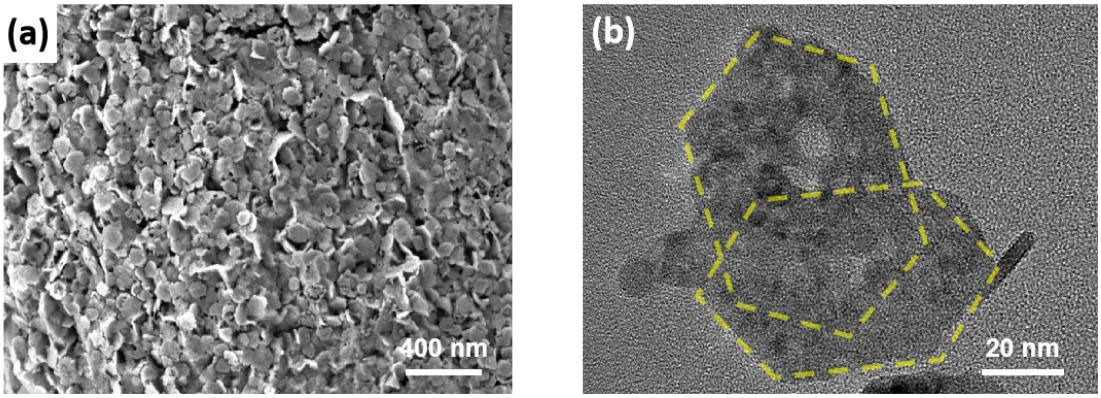

Figure S18. (a) SEM and (b) TEM images of CdO-$Co_{3-x}Cd_xO_4$

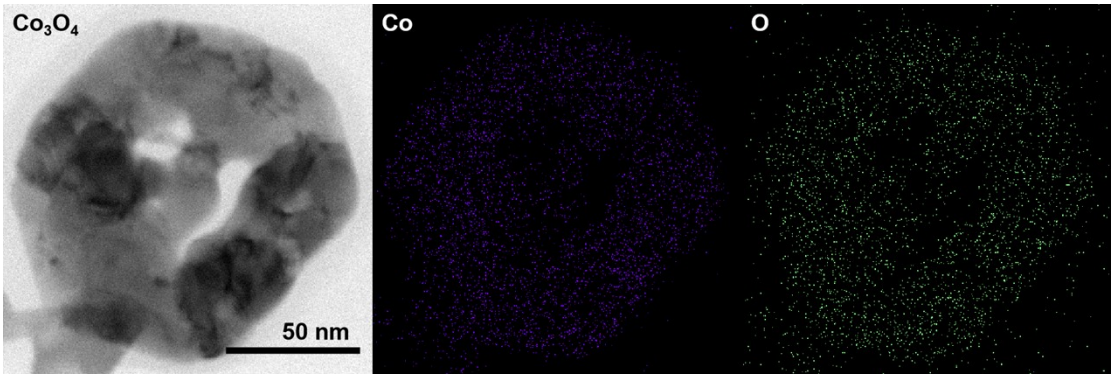

Figure S19. EDS with elemental mapping images of Co_3O_4.

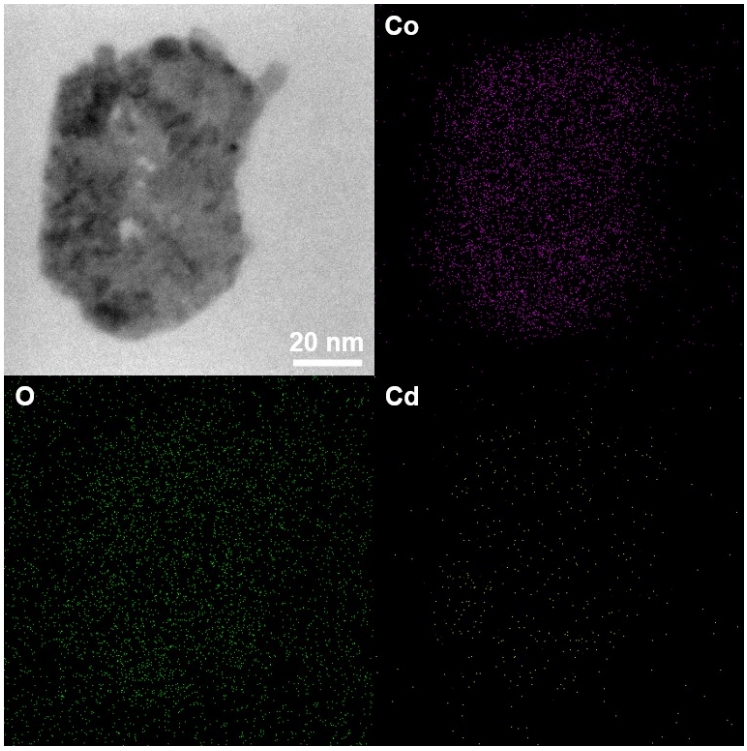

Figure S20. TEM with elemental mapping images of CdO-$Co_{3-x}Cd_xO_4$.

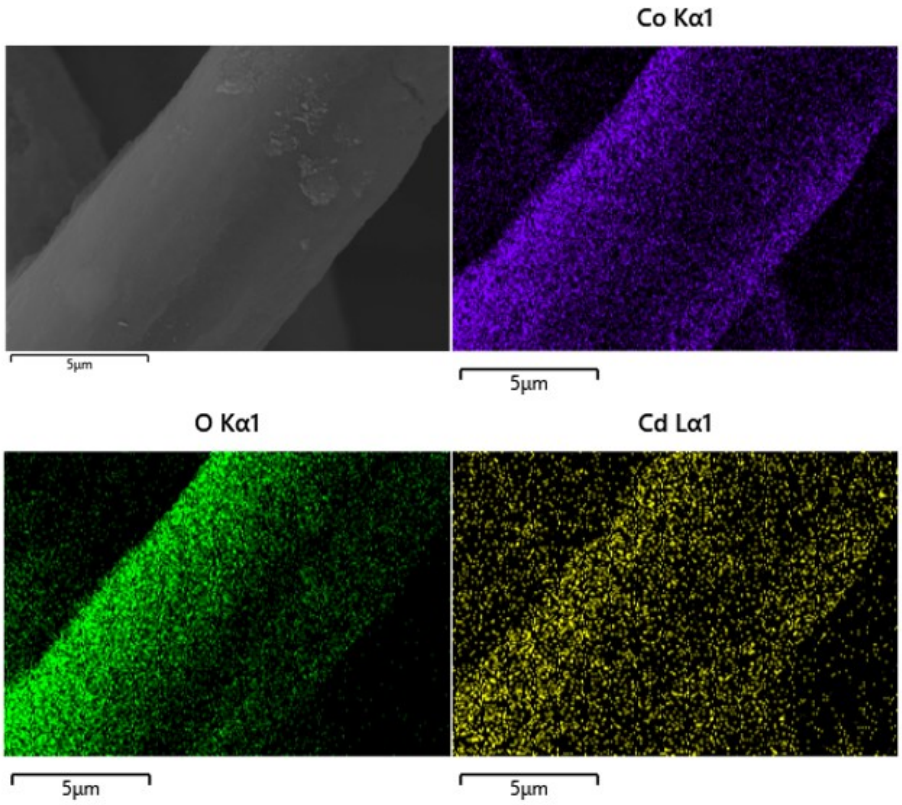

Figure S21. SEM with elemental mapping images of CdO-$Co_{3-x}Cd_xO_4$/CP.

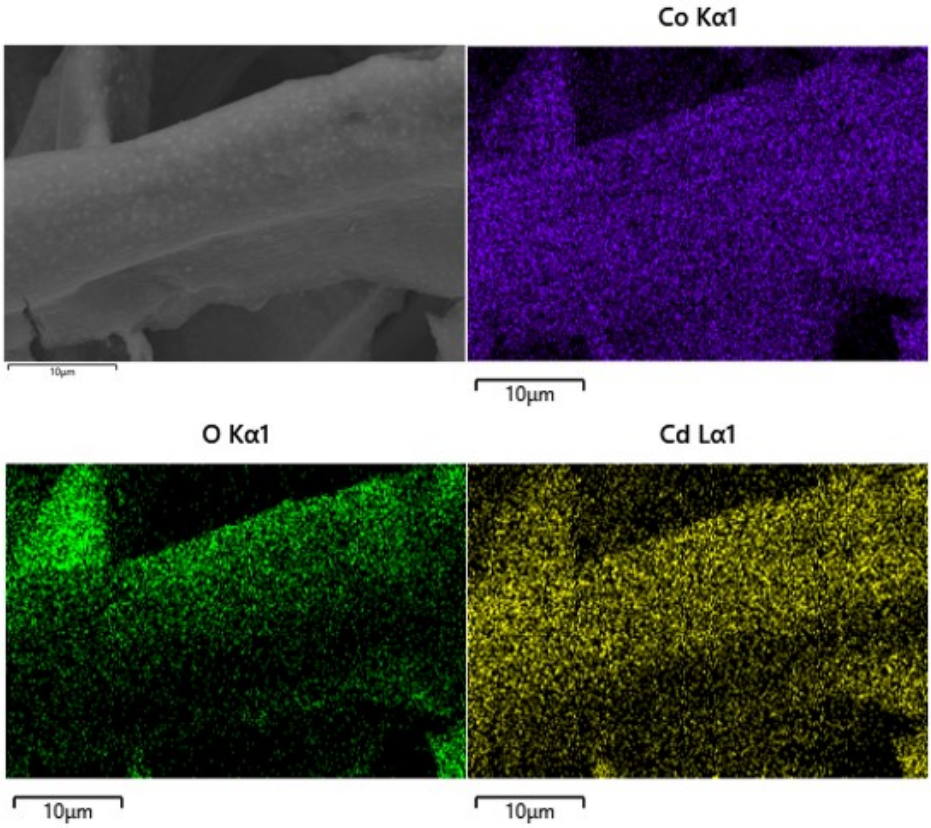

Figure S22. SEM with elemental mapping images of CdO-$Co_{3-x}Cd_xO_4$/CP after OER.

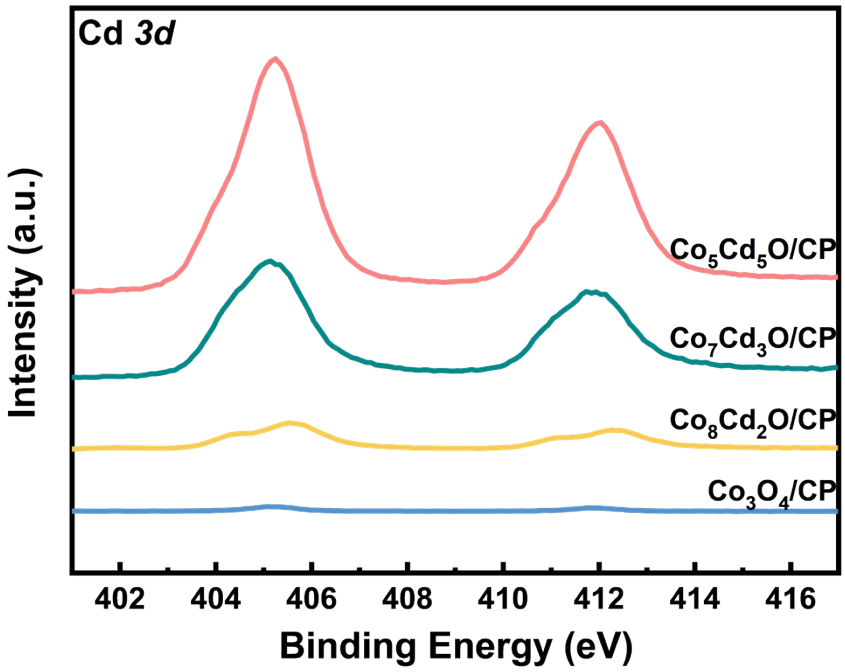

Figure S23. High-resolution XPS spectra of Cd 3d for of Co_3O_4/CP, Co_8Cd_2O/CP, Co_7Cd_3O/CP and Co_5Cd_5O/CP.

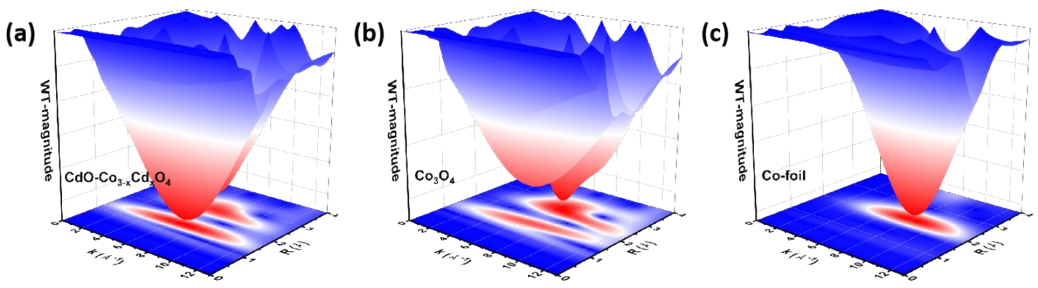

Figure S24. Corresponding wavelet-transformed EXAFS spectra of $CdO\text{-}Co_{3\text{-}x}Cd_xO_4$ (a), Co_3O_4 (b), and Co foil (c).

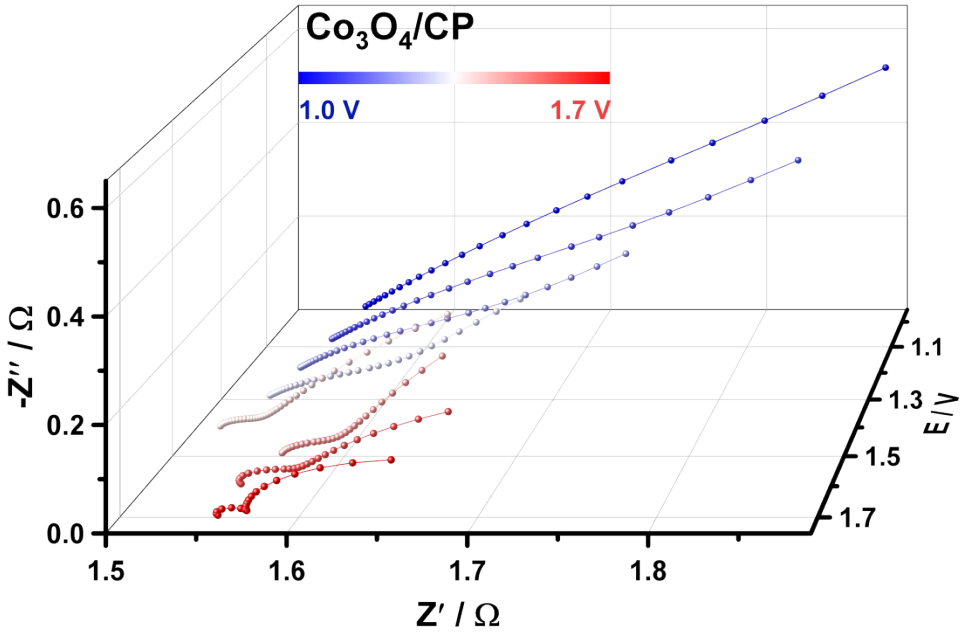

Figure S25. The Nyquist plots of Co_3O_4/CP at different applied potentials.

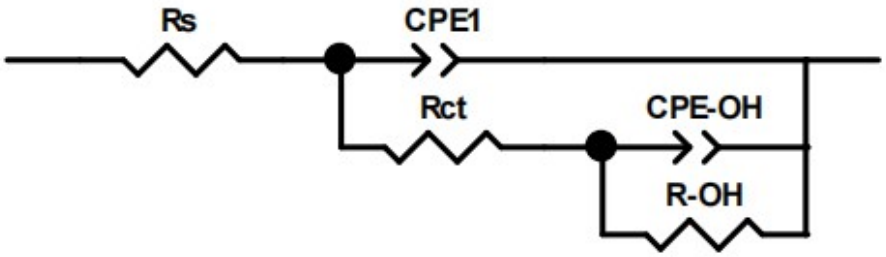

Figure S26. The equivalent circuit used for modeling the electrochemical impedance spectra.

Rs represents solution resistance. Rct and R-OH are related with the interface reaction charge transfer resistances and resistances of the intermediate accumulation. CPE1 and CPE-OH are represented the double layer capacitance and the relaxation of the charge associated with adsorbed intermediate.

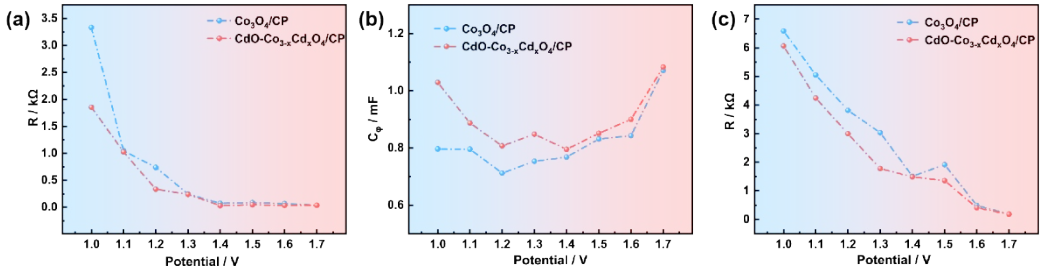

Figure S27. (a) The extracted Rct plots at different appliedpotential, (b) The extracted CPE-OH plots at different appliedpotential, (c) The extracted R-OH plots at different appliedpotential.

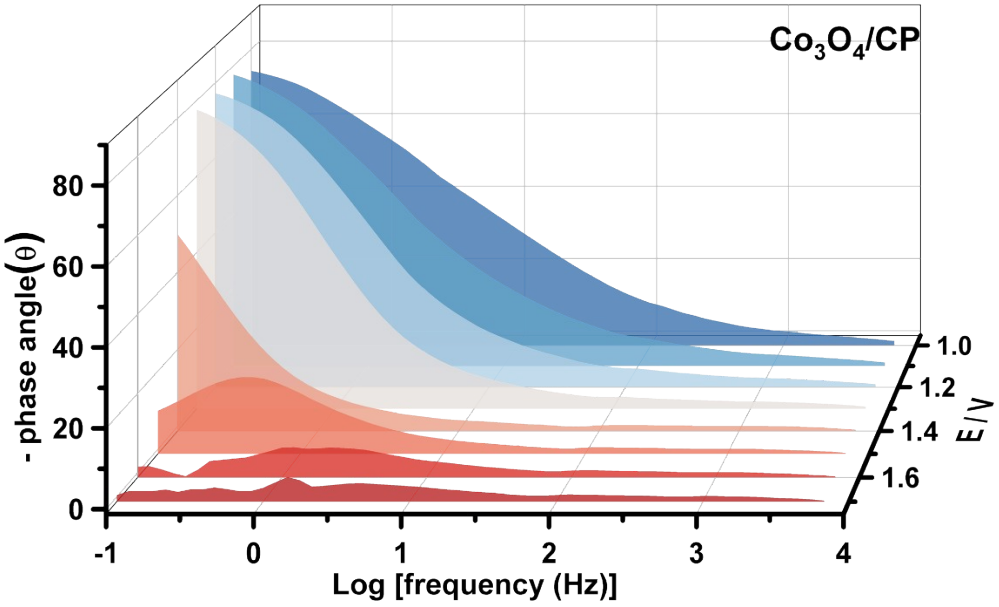

Figure S28. Bode phase plots of Co_3O_4/CP at different applied potential.

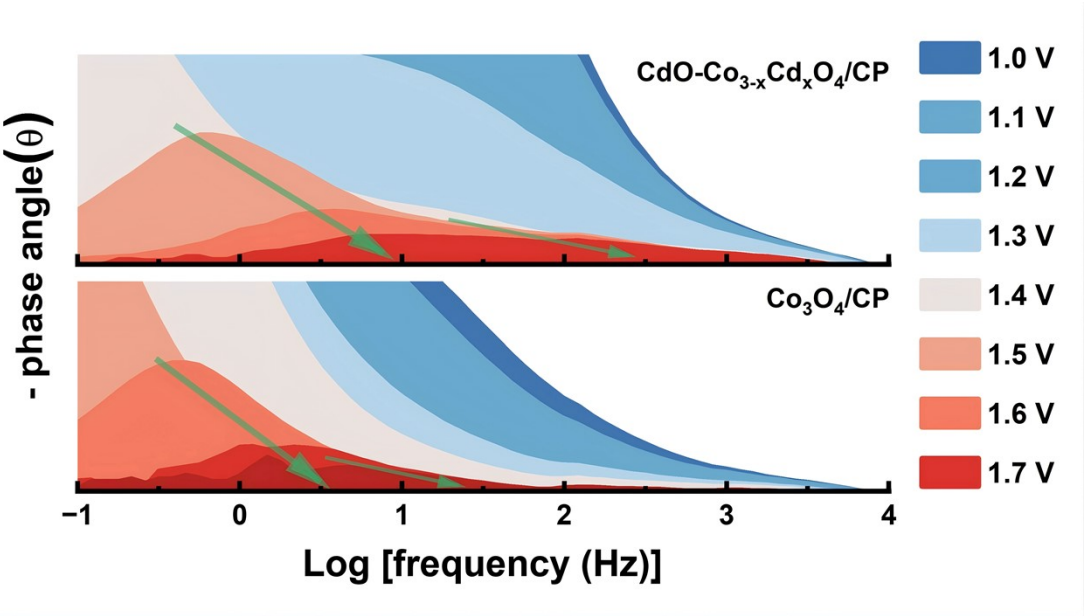

Figure S29. Bode phase plots of CdO-$Co_{3-x}Cd_xO_4$/CP and Co_3O_4/CP at different applied potential.

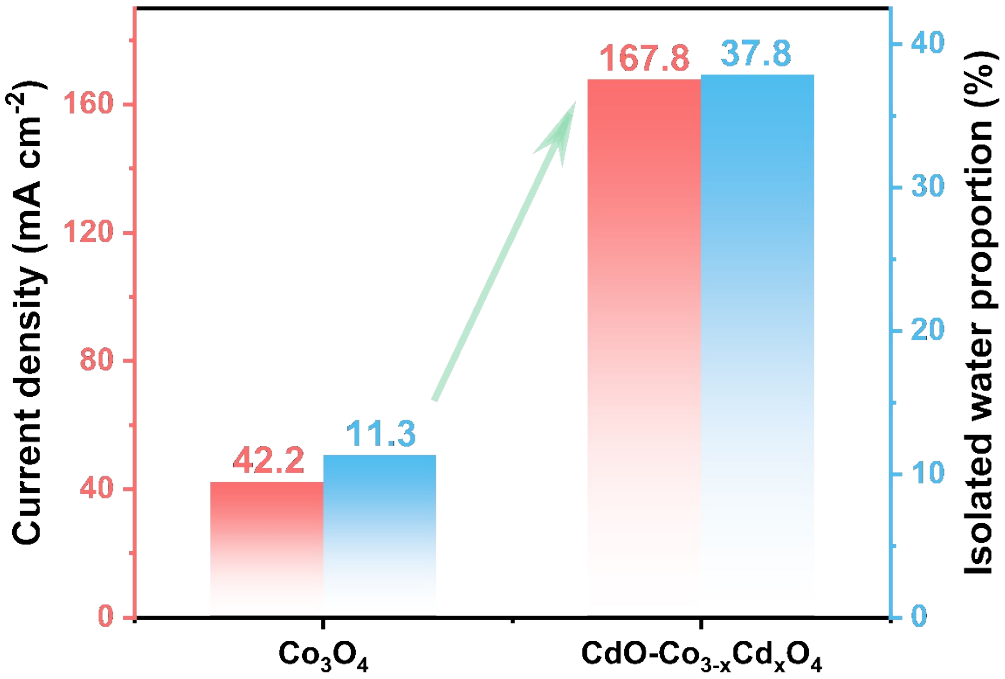

Figure S30. The relationship graph between the current density of the catalyst and the proportion of isolated water at 1.7 V.

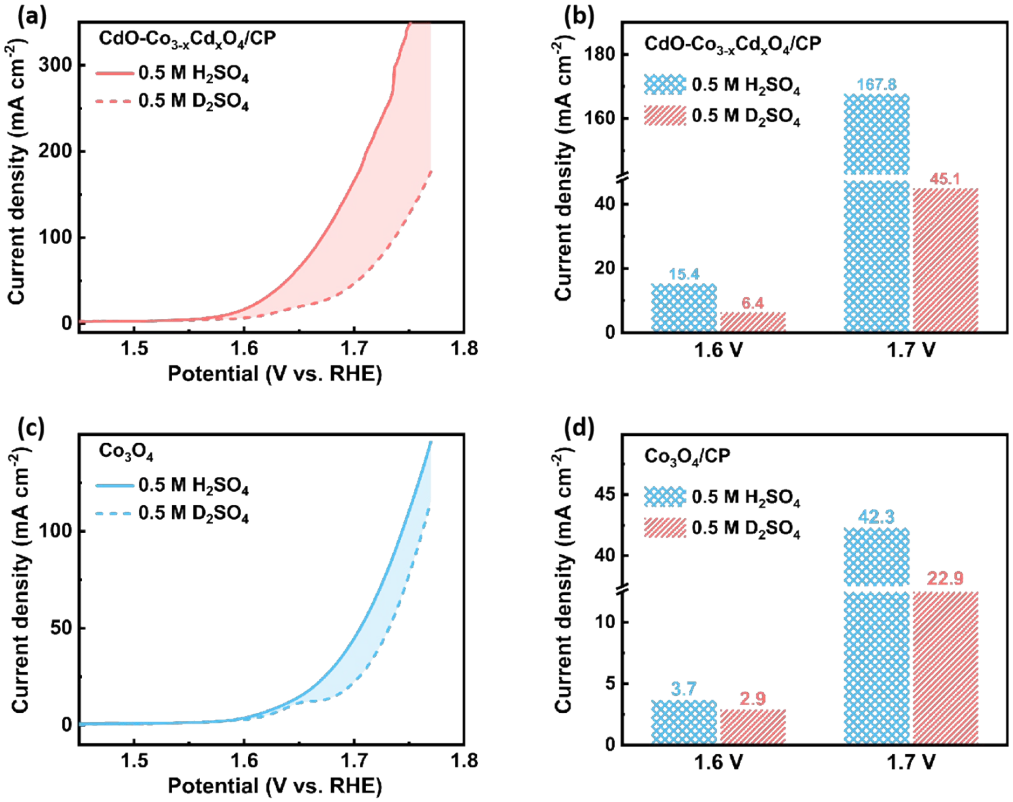

Figure S31. The H/D isotope substitution to study the OER reaction kinetics of the catalyst. (a, b) The LSV curves of CdO-$Co_{3-x}Cd_xO_4$/CP, (c, d) the LSV curves of Co_3O_4/CP recorded in the acidic (0.5 M H_2SO_4 in H_2O; 0.5 M D_2SO_4 in D_2O).

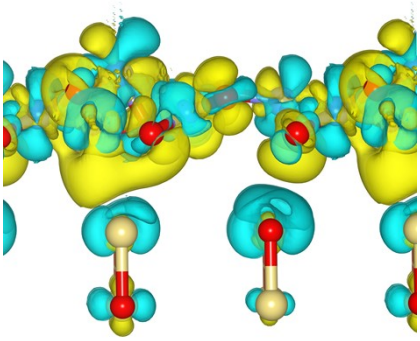

Figure S32. The differential charge density of CdO-$Co_{3-x}Cd_xO_4$.

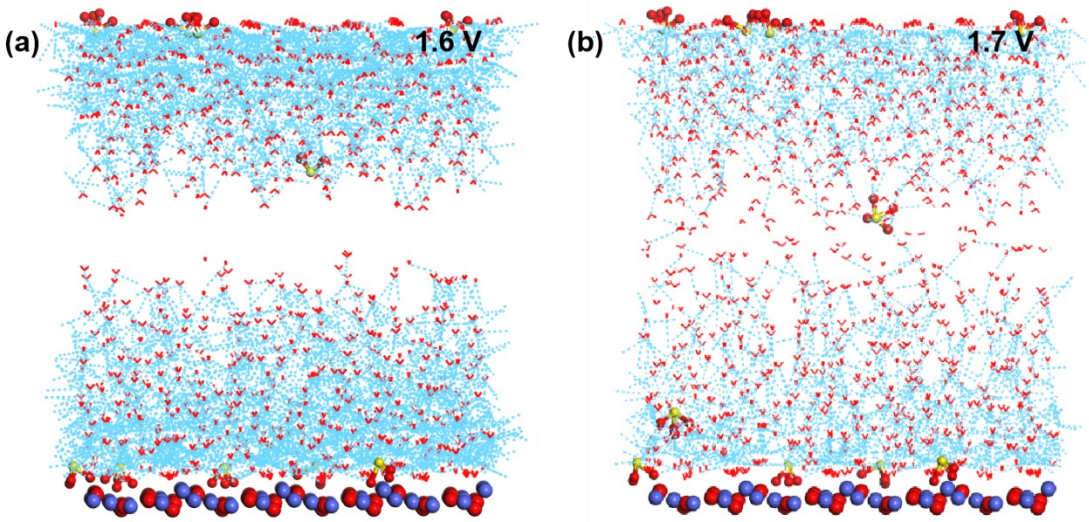

Figure S33. Representative snapshots with H-bond of the interfacial water substructure of Co_3O_4 are at 1.6 V (a) and 1.7 V (b).

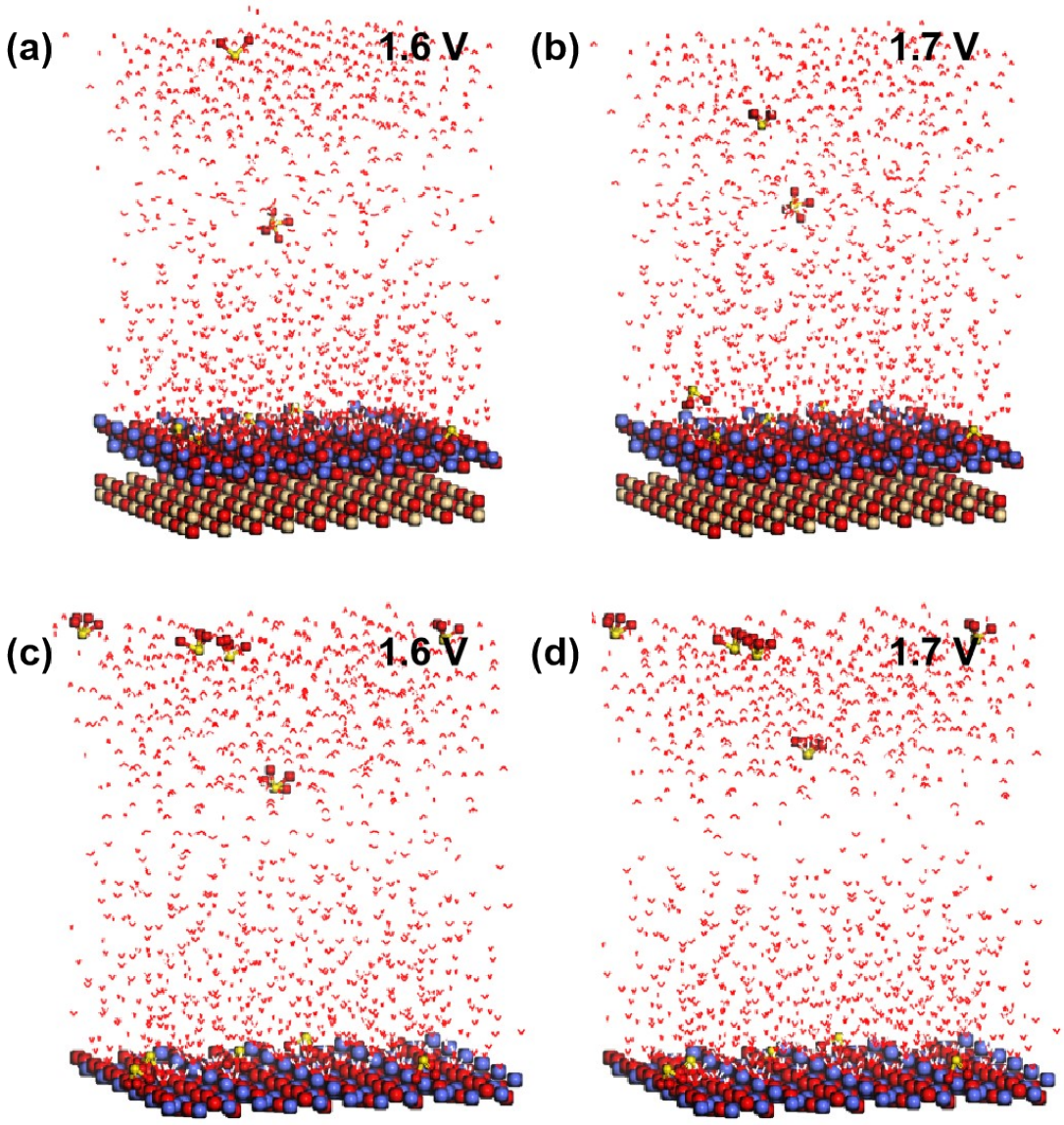

Figure S34. Representative snapshots of the interfacial water substructure of CdO-$Co_{3-x}Cd_xO_4$ (a and b) and Co_3O_4 (c and d) at 1.6 V and 1.7 V.

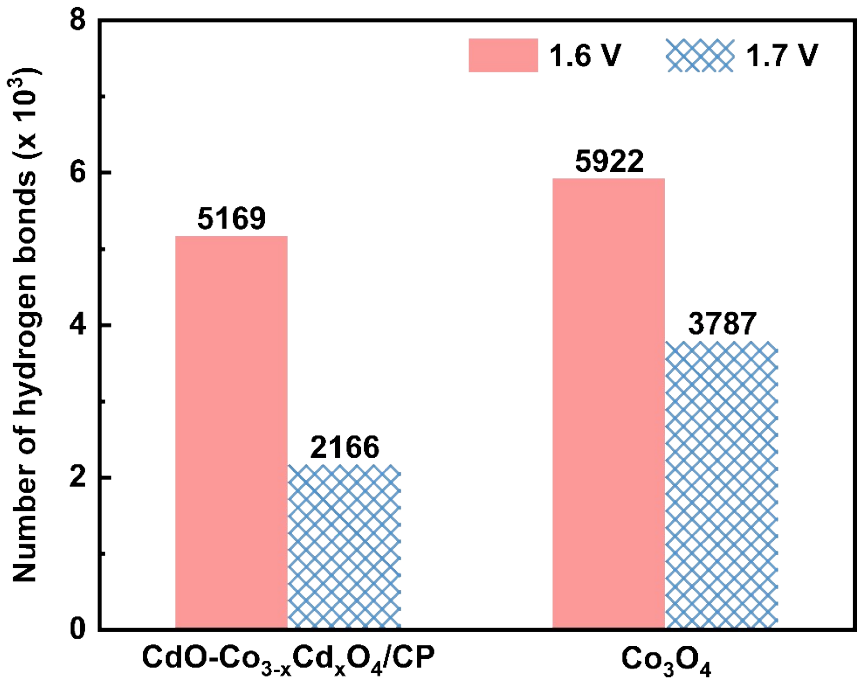

Figure S35. The average number of hydrogen bonds at the catalyst interface at 1.6 V and 1.7 V.

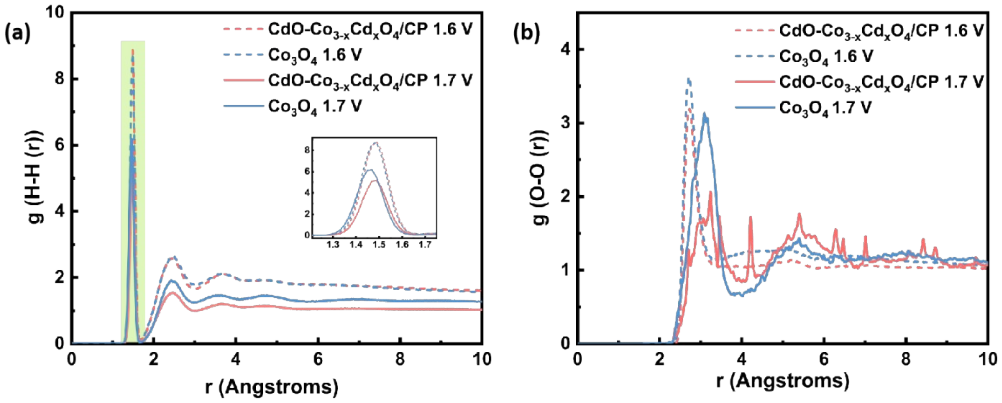

Figure S36. (a)The RDF $g_{H-H}(r)$ between H and H atoms of the water interface and (b) The RDF $g_{O-O}(r)$ between O and O atoms of the water interface at 1.6 V and 1.7 V.

Table S1. Atomic ratio of Co/Cd in CdO-$Co_{3-x}Cd_xO_4$/CP determined by EDS and ICP-MS.

Method	Co (at. %)	Cd (at. %)	O (at. %)
EDS	32.08	7.30	49.84
ICP-MS	65.32	34.68	--

Table S2. Properties of non-precious metal OER catalysts from this work and other typical literature.

Catalyst	Electrolyte	Overpotential @ 10 mA cm^{-2} (mV)	Stability @ 10 mA cm^{-2} (h)	Reference
CoFeNiMoWTe	0.5 M H_2SO_4	395	100	[1]
Fe-Co_3O_4@C/FTO	0.5 M H_2SO_4	396	50	[2]
Co_3O_4/CeO_2	0.5 M H_2SO_4	347	50	[3]
P-Co_3O_4	0.5 M H_2SO_4	400	30	[4]
Mo-Co_9S_8@C	0.5 M H_2SO_4	370	24	[5]
La- and Mn-Codoped porous cobalt spinel fibers	0.5 M H_2SO_4	353	360	[6]
$Ta_1Co_{3-x}O_4$	0.05 M H_2SO_4	378	140	[7]
Na-treated Mesoporous Co_3O_4	0.5 M H_2SO_4	412	9	[8]
$Co_3O_{4-x}F_x$	0.5 M H_2SO_4	349	120	[9]
Co_2MnO_4 on FTO	0.5 M H_2SO_4	395	320	[10]
CoSAs-MoS_2/TiN NRs	0.5 M H_2SO_4	454	24	[11]
Ba [Co-POM]	0.5 M H_2SO_4	361	24	[12]
c-Co_3O_4@NFs	0.5 M H_2SO_4	377	24	[13]
HSS-CoO_x/GDY	0.5 M H_2SO_4	221	400	[14]
Cr-Co_3O_4	0.5 M H_2SO_4	358	160	[15]
Sm–$MnCo_2O_{4.5}$	0.5 M H_2SO_4	212	1200	[16]
W-$NiCo_2O_4$	0.5 M H_2SO_4	289	600	[17]
CdO-$Co_{3-x}Cd_xO_4$/CP	0.5 M H_2SO_4	346	90	This work

Table S4. Fitting information of in-situ ATR-SEIRAS spectra of CdO-$Co_{3-x}Cd_xO$ under different applied potentials (1.0-1.7 V vs. RHE).

Applied potential	Peak	Position	Intensity	Area	FWHM	R^2
1.0 V	Peak 1	3200.58233	0.00879	1.51263	161.23787	0.99629
	Peak 2	3352.71119	0.01096	2.81587	224.25254	
	Peak 3	3499.36547	0.0036	0.73813	227.02467	
1.1 V	Peak 1	3200.58233	0.00886	1.52337	161.23787	0.99631
	Peak 2	3352.71119	0.01023	2.50118	224.25254	
	Peak 3	3499.36547	0.00497	1.13847	227.02467	
1.2 V	Peak 1	3201.11226	0.00929	1.56145	161.80543	0.99610
	Peak 2	3361.62162	0.01131	2.8889	229.82243	
	Peak 3	3512.81836	0.00503	1.17684	215.15204	
1.3 V	Peak 1	3201.68229	0.01005	1.70453	161.97395	0.99617
	Peak 2	3373.93954	0.01235	3.24127	241.44387	
	Peak 3	3530.99528	0.00523	1.25899	192.48335	
1.4 V	Peak 1	3200.02259	0.00882	1.51116	158.19226	0.99549
	Peak 2	3360.52338	0.00949	2.26477	240.11359	
	Peak 3	3514.24701	0.00582	1.40472	220.16184	
1.5 V	Peak 1	3200.08533	0.00913	1.6456	159.97293	0.99599
	Peak 2	3345.21006	0.00847	2.20359	218.62611	
	Peak 3	3487.14023	0.00636	1.74565	232.50161	
1.6 V	Peak 1	3199.2602	0.00968	1.82678	159.58859	0.99584
	Peak 2	3360.98289	0.00947	2.49256	246.64472	
	Peak 3	3515.2538	0.00706	1.8129	226.55176	
1.7 V	Peak 1	3200.4952	0.01064	1.76163	161.61006	0.99528
	Peak 2	3349.173	0.0105	2.00045	223.05097	
	Peak 3	3498.99954	0.00723	2.29433	235.70644	

- The characteristic peaks fitted in the range of 3000-3800 cm^{-1} in the in-situ ATR-SEIRAS spectra are designated as Peak 1, Peak 2, and Peak 3 in order of increasing wavenumber.
- FWHM represents Full Width at Half Maximum.
- R^2 represents the coefficient of determination.

In the in-situ ATR-SEIRAS analysis, we used Origin software to perform Gaussian peak fitting on the O-H vibration band of water molecules in the range of 3000 to 3800 cm^{-1} to minimize random residuals. For baseline correction, the linear baseline correction method was employed to effectively eliminate background signals. The fitted parameters, including peak position, intensity, peak area, full width at half maximum (FWHM), and their corresponding standard errors, were systematically listed in Supplementary Tables S4 and S5.

Table S5. Fitting information of in-situ ATR-SEIRAS spectra of Co_3O_4 under different applied potentials (1.0-1.7 V vs. RHE).

Applied potential	Peak	Position	Intensity	Area	FWHM	R^2
1.0 V	Peak 1	3212.25217	0.01456	2.52383	163.03141	0.99405
	Peak 2	3403.77043	0.0185	4.74274	240.91268	
	Peak 3	3557.70557	0.00535	0.87012	152.85197	
1.1 V	Peak 1	3212.3539	0.01526	2.72624	168.06976	0.99476
	Peak 2	3407.34529	0.01896	4.8993	242.79159	
	Peak 3	3562.30402	0.00497	0.79583	150.40017	
1.2 V	Peak 1	3211.29494	0.01504	2.59501	162.24852	0.99379
	Peak 2	3402.07398	0.01887	4.89239	243.56575	
	Peak 3	3557.68579	0.0052	0.85119	153.83068	
1.3 V	Peak 1	3211.16281	0.01539	2.68654	164.21651	0.99359
	Peak 2	3402.1187	0.01877	4.85074	242.7473	
	Peak 3	3558.12656	0.00506	0.82132	152.43754	
1.4 V	Peak 1	3211.16281	0.01539	2.68654	164.21651	0.99367
	Peak 2	3402.1187	0.01877	4.85074	242.7473	
	Peak 3	3558.12656	0.00506	0.82132	152.43754	
1.5 V	Peak 1	3210.57577	0.0152	2.62162	162.18292	0.99328
	Peak 2	3398.90634	0.01844	4.73396	241.15534	
	Peak 3	3553.93377	0.00524	0.85836	153.86141	
1.6 V	Peak 1	3210.65237	0.01553	2.67819	162.2015	0.99347
	Peak 2	3398.83959	0.01847	4.71295	239.73851	
	Peak 3	3553.83387	0.00516	0.83518	151.94734	
1.7 V	Peak 1	3210.37053	0.01544	2.65576	161.75517	0.99323
	Peak 2	3396.7896	0.01801	4.5567	237.69759	
	Peak 3	3550.76105	0.00524	0.85889	154.03752	

Reference

1. Jo, S.; Kim, M.-C.; Lee, K. B.; Choi, H.; Zhang, L.; Sohn, J. I., Nonprecious High-Entropy Chalcogenide Glasses-Based Electrocatalysts for Efficient and Stable Acidic Oxygen Evolution Reaction in Proton Exchange Membrane Water Electrolysis. *Adv. Energy Mater.* **2023**, *13*, 2301420.

2. Senthil Raja, D.; Cheng, P.-Y.; Cheng, C.-C.; Chang, S.-Q.; Huang, C.-L.; Lu, S.-Y., In-situ grown metal-organic framework-derived carbon-coated Fe-doped cobalt oxide nanocomposite on fluorine-doped tin oxide glass for acidic oxygen evolution reaction. *Appl. Catal., B* **2022**, *303*, 120899.

3. Huang, J.; Sheng, H.; Ross, R. D.; Han, J.; Wang, X.; Song, B.; Jin, S., Modifying redox properties and local bonding of Co_3O_4 by CeO_2 enhances oxygen evolution catalysis in acid. *Nat. Commun.* **2021**, *12*, 3036.

4. Shang, F.; He, H.; Li, P.; Cai, H.; An, B.; Li, X.; Yang, S.; Sun, Z.; Wang, B., PO_6 geometric configuration unit enhanced electrocatalytic performance of Co_3O_4 in acidic oxygen evolution. *J. Colloid Interface Sci.* **2023**, *641*, 329-337.

5. Wang, L.; Duan, X.; Liu, X.; Gu, J.; Si, R.; Qiu, Y.; Qiu, Y.; Shi, D.; Chen, F.; Sun, X.; Lin, J.; Sun, J., Atomically Dispersed Mo Supported on Metallic Co_9S_8 Nanoflakes as an Advanced Noble-Metal-Free Bifunctional Water Splitting Catalyst Working in Universal pH Conditions. *Adv. Energy Mater.* **2020**, *10*, 1903137.

6. Chong, L.; Gao, G.; Wen, J.; Li, H.; Xu, H.; Green, Z.; Sugar, J. D.; Kropf, A. J.; Xu, W.; Lin, X.-M.; Xu, H.; Wang, L.-W.; Liu, D.-J., La- and Mn-doped cobalt spinel oxygen evolution catalyst for proton exchange membrane electrolysis. *Science* **2023**, *380*, 609-616.

7. Lee, K.; Shim, J.; Ji, H.; Kim, J.; Lee, H. S.; Shin, H.; Bootharaju, M. S.; Lee, K.-S.; Ko, W.; Lee, J.; Kim, K.; Yoo, S.; Heo, S.; Ryu, J.; Back, S.; Lee, B.-H.; Sung, Y.-E.; Hyeon, T., Tailoring cobalt spinel oxide with site-specific single atom incorporation for high-performance electrocatalysis. *Energy Environ. Sci.* **2024**, *17*, 3618-3628.

8. Zhu, Y.; Wang, J.; Koketsu, T.; Kroschel, M.; Chen, J.-M.; Hsu, S.-Y.; Henkelman, G.; Hu, Z.; Strasser, P.; Ma, J., Iridium single atoms incorporated in Co_3O_4 efficiently catalyze the oxygen evolution in acidic conditions. *Nat. Commun.* **2022**, *13*, 7754.

9. Wang, Y.; Guo, P.; Zhou, J.; Bai, B.; Li, Y.; Li, M.; Das, P.; Wu, X.; Zhang, L.; Cui, Y.; Xiao, J.; Wu, Z.-S., Tuning the Co pre-oxidation process of Co_3O_4via

geometrically reconstructed F–Co–O active sites for boosting acidic water oxidation. *Energy Environ. Sci.* **2024**, *17*, 8820-8828.

10. Li, A.; Kong, S.; Guo, C.; Ooka, H.; Adachi, K.; Hashizume, D.; Jiang, Q.; Han, H.; Xiao, J.; Nakamura, R., Enhancing the stability of cobalt spinel oxide towards sustainable oxygen evolution in acid. *Nat. Catal.* **2022**, *5*, 109-118.

11. Wang, X.; Zhong, H.; Xi, S.; Lee, W. S. V.; Xue, J., Understanding of Oxygen Redox in the Oxygen Evolution Reaction. *Adv. Mater.* **2022**, *34*, 2107956.

12. Blasco-Ahicart, M.; Soriano-López, J.; Carbó, J. J.; Poblet, J. M.; Galan-Mascaros, J. R., Polyoxometalate electrocatalysts based on earth-abundant metals for efficient water oxidation in acidic media. *Nat. Chem.* **2018**, *10*, 24-30.

13. Tang, Y.; Liang, N.-N.; Li, Y.; Luo, Q.; Ding, W.; Li, B.; Gao, X.; Pang, Q.; Ji, D.; Luo, M., Confined Kirkendall Strain Engineering Promotes Oxygen Evolution on Co_3O_4 for Proton Exchange Membrane Water Electrolyzer. *Adv. Energy Mater.* **2026**, e06692. https://doi.org/10.1002/aenm.202506692

14. Ping, X.; Xue, Y.; Chen, S.; Zheng, Y.; Chen, S.; Gao, Y.; Li, Y., High-spin transition metal atoms drive acidic oxygen evolution reactions. *Nat. Commun.* **2026**. https://doi.org/10.1038/s41467-026-69682-9

15. Wu, L.; Zhao, B.; Huang, W.; Li, D.; Liao, Z.; Chen, Y.; Yao, N.; Zhou, H.; Luo, W., Dynamic chromium dopant promotes interfacial water activation on cobalt spinel oxide for efficient oxygen evolution in acid. *Nat. Commun.* **2026**. https://doi.org/10.1038/s41467-026-69124-6

16. Li, M.; Yang, J.; Li, S.; Deng, L.; Zhao, S.; Li, L.; Hung, S.-F.; Xing, G.; Wang, T.; Liang, Y.; Ren, J.; Wu, Y.; Peng, S., Rare-Earth-Induced Intermediate-Spin Co Centers in $MnCo_2O_{4.5}$ for Sustainable Acidic Water Oxidation. *J. Am. Chem. Soc.* **2025**, *147*, 45680-45690.

17. Li, S.; Zhao, S.; Hung, S.-F.; Deng, L.; Wang, L.; Shi, F.; Dong, A.; Zhang, Y.; Chen, T.-Y.; Hu, F.; Li, L.; Ramakrishna, S.; Wu, Y.; Peng, S., Oxophilic Sites Mediated Dynamic Oxygen Replenishment to Stabilize Lattice Oxygen Catalysis in Acidic Water Oxidation. *J. Am. Chem. Soc.* **2025**, *147*, 33770-33779.